



Article

Calculation Model of Radar Terrain Masking Based on Tensor Grid Dilation Operator

Kaiyu Nie^{1,2}, Shengliang Fang³, Hao Liu^{4,5}, Xiaofeng Wei^{1,2}, Yamin Zhang^{1,2}, Jianpeng Yang⁶, Qinglei Kong^{1,2} 
and Bo Chen^{1,2,*}

¹ Institute of Space Science and Applied Technology, Harbin Institute of Technology (Shenzhen), Shenzhen 518055, China; 22s061021@stu.hit.edu.cn (K.N.); weixiaofeng@pku.edu.cn (X.W.); zhangyamin@stu.hit.edu.cn (Y.Z.); kongqinglei@hit.edu.cn (Q.K.)

² Key Laboratory of Aerospace RS Big-Data Intelligent Processing and Application of Guangdong Higher Education Institutes, Harbin Institute of Technology (Shenzhen), Shenzhen 518055, China

³ College of Aerospace Information, Space Engineering University, Beijing 101416, China; eeifslyl@163.com

⁴ School of Electronic Information and Electrical Engineering, Shanghai Jiao Tong University, Shanghai 200240, China; liuhao2020@sjtu.edu.cn

⁵ Wuhan Institute of Digital Engineering, Wuhan 430205, China

⁶ ShanDong StarSAT Technology Co., Ltd., Yantai 264000, China; yangjp_dm@126.com

* Correspondence: hitchenbo@hit.edu.cn

Abstract: In recent years, the three-dimensional (3D) radar detection range has played an essential role in the layout of devices such as aircraft and drones. To compensate for the shortcomings of three-dimensional calculations for radar terrain masking, a new calculation method is proposed for assessing the terrain occlusion of radar detection range. First, the high-dimensional electromagnetic data after discretization are modeled based on the tensor data structure, and the tensor grid dilation operator is constructed. Then, the dilation process begins from the overlapping section of the radar detection range and terrain, and it is adjusted by the terrain occlusion judgment factor and the dilation judgment factor to obtain the obstructed part due to the terrain. Finally, the actual radar detection range under terrain occlusion is obtained. The simulation results show that the method proposed in this paper can adapt to different grid sizes and terrain shapes, significantly enhancing computational efficiency while maintaining internal features.

Keywords: three-dimensional radar detection range; terrain masking; dilation



Citation: Nie, K.; Fang, S.; Liu, H.; Wei, X.; Zhang, Y.; Yang, J.; Kong, Q.; Chen, B. Calculation Model of Radar Terrain Masking Based on Tensor Grid Dilation Operator. *Remote Sens.* **2024**, *16*, 1432. <https://doi.org/10.3390/rs16081432>

Academic Editor: Timo Balz

Received: 5 March 2024

Revised: 13 April 2024

Accepted: 15 April 2024

Published: 18 April 2024



Copyright: © 2024 by the authors. Licensee MDPI, Basel, Switzerland. This article is an open access article distributed under the terms and conditions of the Creative Commons Attribution (CC BY) license (<https://creativecommons.org/licenses/by/4.0/>).

1. Introduction

Radar is a kind of radio detection equipment that utilizes the scattering and reflection of electromagnetic waves to detect targets. It has extensive applications in both military and civilian fields, including target search, tracking, and surveillance in the military sector, as well as air traffic control, weather detection, and unmanned environmental perception in civilian applications. In modern warfare, the 3D coverage of radar is of great concern. The radar coverage is influenced by factors such as terrain, Earth's curvature, atmosphere, and ground clutter, with terrain masking being the most significant factor. Therefore, it is of crucial importance to accurately calculate the actual 3D radar detection range under terrain obstruction. Currently, the calculation methods for radar coverage can be mainly divided into mathematical modeling methods and geometric modeling methods.

The mathematical modeling methods mainly consider the influence of multiple environmental factors on the radar detection range. Chen et al. [1] proposed a three-dimensional modeling method of the radar detection range based on the parabolic equation, which considered the influence of multiple factors on the detection range. Cheng et al. [2] quantitatively analyzed various factors, including weather, interference, and target height. They designed a Back Propagation (BP) neural network and trained it with a large amount

of sample data, enabling the calculation of actual radar detection ranges under various conditions. In recent years, a wealth of measured data has also been used to correct radar detection range [3]. However, these methods required access to a large amount of data and did not consider the influence of terrain. In summary, the advantages of mathematical modeling methods lie in their consideration of more environmental influences. However, their shortcomings entail having a high computational complexity and often not being able to solve the problem of terrain occlusion well.

Geometric modeling methods consider the impact of terrain occlusion. A commonly used approach is to sample along the azimuth direction at regular intervals, discretize the radar detection range boundary in the vertical profile corresponding to each azimuth, and then correct the boundary based on the ray propagation method according to the terrain [4]. To reduce computational overhead, Qiu et al. [5] proposed a hybrid sampling method that utilized non-uniform sampling in the radar elevation direction. They also explored the relationship between visualization rendering efficiency and accuracy in different scenarios and further analyzed the reasons behind it [6]. Sampling along horizontal profiles at specific elevations is also a common method. Zhang et al. [7] determined the existence of terrain masking for each sampling point in the horizontal profile through the triangle primitive intersection algorithm. Liu et al. [8] proposed a line-of-sight visibility detection method, which determined whether the target was obscured by comparing the target elevation angle with the terrain elevation angle. Dong et al. [9] defined the radar minimum visible angle and calculated the detection range at different altitudes based on the Earth's curvature. The main issue with geometric modeling methods is that their 3D radar detection range calculations are still calculated within two-dimensional cross-sections, leading to some computational redundancies. A new method is to discretize the radar detection range based on a grid subdivision algorithm and encode the radar detection range and terrain data, thus converting the complex computation into the intersection operation of the encoded set, which is relatively simple to compute [10]. However, the algorithm only considers the scenario where the radar beam is completely occluded by terrain and does not consider the case where the terrain partially obstructs the radar beam. Therefore, further research is still needed in this regard.

To directly compute radar terrain occlusion in a three-dimensional space, this paper proposes a calculation model of radar terrain masking based on a tensor grid dilation operator. Based on the concept of grid subdivision, high-dimensional electromagnetic data and terrain data are discretized, and a high-dimensional electromagnetic data tensor grid model is constructed. The terrain masking is then computed using the idea of dilation operation in morphology. The algorithm focuses on the radar detection range's internal characteristics while considering the calculation efficiency. The overall research framework of the paper is shown in Figure 1.

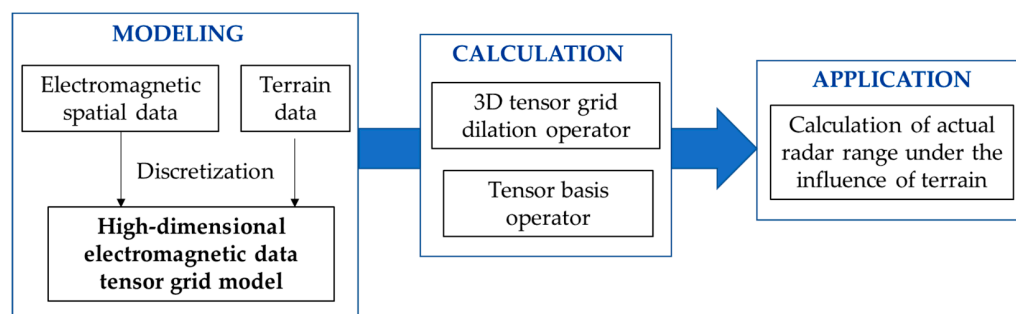


Figure 1. The overall research framework of the paper.

The structure of this paper is as follows: Section 2 explains the tensor model and related fundamental operations. Section 3 focuses on the tensor grid-based modeling of high-dimensional electromagnetic data and the definition of the tensor grid dilation operator. Section 4 elaborates on the construction of the radar terrain masking calculation

algorithm based on the 3D tensor grid dilation operator, including specific processes. Sections 5 and 6 present the experimental results and conclusions, respectively.

2. Related Works

In this paper, electromagnetic space data are mainly modeled based on the tensor, and this section provides an explanation of the tensor and its application to spatio-temporal data.

2.1. Tensor and Its Application to Spatio-Temporal Data

Tensors are generalizations of vectors and matrices to higher orders and higher dimensional [11], which can maintain the underlying structure of complex data and represent high-dimensional, diverse, and massive data well. By utilizing the high-dimensional representation properties and coordinate invariance of tensors, it is possible to model multidimensional data effectively. Therefore, modeling high-dimensional electromagnetic data based on tensors is of significant importance for discrete electromagnetic computations.

In recent years, tensors have been widely used in spatio-temporal data analysis, such as time series data prediction, spatiotemporal data interpolation, spatio-temporal correlation analysis, etc. Li et al. [12] proposed a tensor-based irregular spatio-temporal field data model, which can store and calculate multidimensional geographic spatio-temporal field data and can realize data compression, retrieval, recombination, and other operations. Zhang et al. [13] proposed a spatio-temporal tensor model based on spatio-temporal correlation priors, to simultaneously utilize the spatial and temporal information of infrared video backgrounds, thereby achieving target-background separation. Liu et al. [14] modeled five-dimensional (5D) seismic data and successfully reconstructed seismic data based on tensor train decomposition and tensor ring decomposition.

In the field of electromagnetic data, using tensor modeling in Multiple-Input Multiple-Output (MIMO) systems has been shown to have potential in achieving high spectral efficiencies by exploiting spatial and code multiplexing [15]. Zhai et al. [16] organized spectrum data into a spectrum tensor from three dimensions of time, space, and frequency. Also, they conducted a study on multi-dimensional spectral data denoising based on the tensor decomposition model. Cai [17] organized the electromagnetic information of the local area into a multi-level ordered tensor form using the spatial subdividing method and further provided an efficient method of retrieval and dimension expansion.

2.2. Basic Operations on Tensor

Since it is relatively difficult to represent tensors of order four or higher graphically, we will use a third-order tensor as an example to introduce the two fundamental operations of tensors. Figure 2 shows the schematic of a third-order tensor, with the size of each dimension to five; in this case, there is $\mathcal{X} \in R^{I_1 \times I_2 \times I_3}$, $I_1 = I_2 = I_3 = 5$.

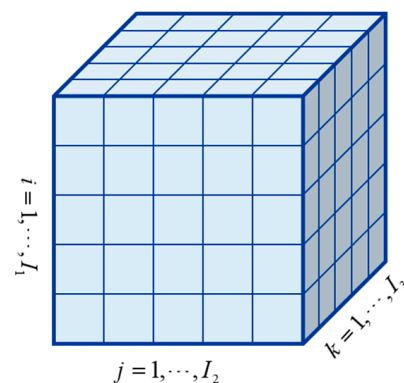


Figure 2. Schematic of the third-order tensor.

(a) Fiber

The fiber is a one-dimensional unfolding structure of a tensor along a specific direction, usually represented as a vector. For the tensor $\mathcal{X} \in R^{n_1 \times \dots \times n_d}$, its fiber is defined by fixing every index but one [18]. Typically, for a third-order tensor, its mode-1 fiber is called the column fiber, represented by $x_{:jk}$; the mode-2 fiber is called the row fiber, represented by $x_{i:k}$; and the mode-3 fiber is called the tube fiber, represented by $x_{ij:}$, as shown in Figure 3.

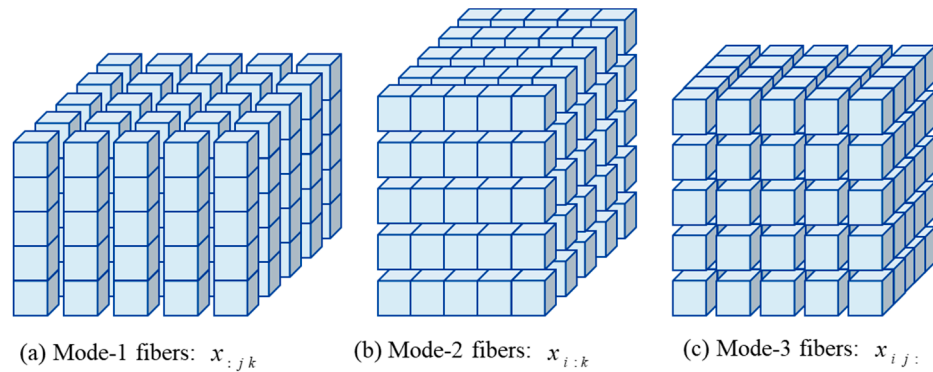


Figure 3. Schematic diagram of the fibers of a third-order tensor.

(b) Slice

Slices are two-dimensional cross-sections of a tensor. For the tensor $\mathcal{X} \in R^{n_1 \times \dots \times n_d}$, it is defined by fixing all but two indices [18]. The remaining two indices are used as row index and column index to form a matrix, which is the slice. Figure 4 shows the horizontal, lateral, and frontal slices of the third-order tensor \mathcal{X} , denoted by $\mathcal{X}(i, :, :)$, $\mathcal{X}(:, j, :)$, and $\mathcal{X}(:, :, k)$, respectively.

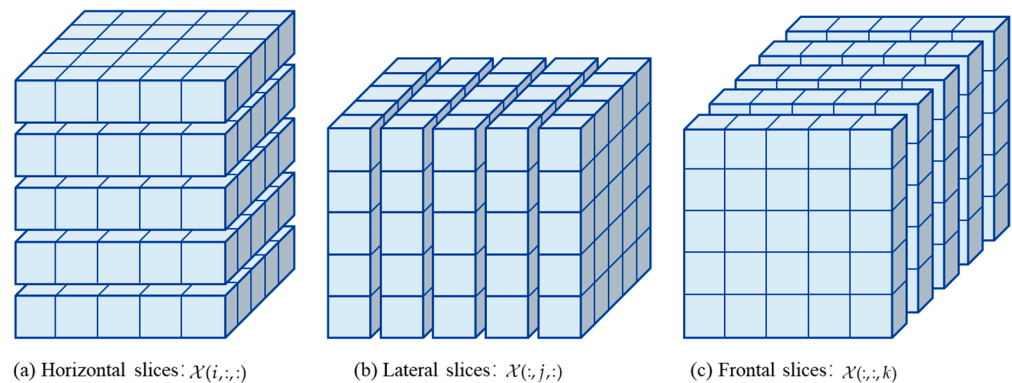


Figure 4. Schematic diagram of slices of a third-order tensor.

3. High-Dimensional Electromagnetic Data Tensor Grid Model

In this section, the discretized high-dimensional electromagnetic data are modeled by selecting appropriate bases to represent the electromagnetic spatial data in tensor form. Then, a 3D tensor grid dilation operator based on the tensor grid model is designed to provide a basis for the subsequent calculation of radar detection range.

3.1. Tensor Grid-Based Modeling of High-Dimensional Electromagnetic Data

Electromagnetic spatial data are a kind of high-dimensional data with spatio-temporal characteristics, which can be organized and represented by the tensor model. The continuous electromagnetic information is discretized based on the grid generation method, and

then a tensor grid model is established with spatial, temporal, and attribute dimensions as bases. Its mathematical definition is as follows:

$$\mathcal{X}_E \in R^{I_1 \times I_2 \times I_3 \times I_4 \times I_P}, \quad (1)$$

\mathcal{X}_E is an electromagnetic data tensor grid model in locally customized spatial settings, in which I_{1-3} represent the size of the three spatial dimensions of longitude, dimension, and height, respectively, I_4 represents the size of the time dimension, and I_P represents the size of the property dimension, which can include the coordinate value, frequency value, power value, polarization angle, detection probability, and other spatial properties and electromagnetic properties. The schematic diagram of the high-dimensional electromagnetic data tensor grid model is shown in Figure 5.

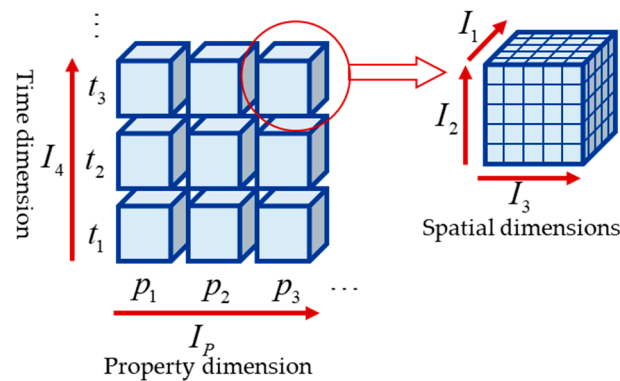


Figure 5. Schematic diagram of the high-dimensional electromagnetic data tensor grid model.

Modeling high-dimensional electromagnetic data using tensors allows for the simultaneous consideration of multiple property dimensions of electromagnetic information, particularly when the position of radiation sources is mobile or the parameters of radiation sources vary over time, enabling time-varying representations. Additionally, since the tensor structure is well-suited for matrix operations, modeling electromagnetic data using tensors makes it more convenient to perform matrix operations, thus effectively boosting computational efficiency.

Since not all dimensions of data will be used in practical calculations, it is feasible to extract several dimensions according to specific requirements. Therefore, this paper extends the tensor slicing operation to higher dimensions and defines it as adaptive dimensional slicing, which can be used for subsequent calculations. For example, if the spatial three-dimensional data, with the property p_1 at a specific time t_2 , are selected to participate in the calculation, then the corresponding portion $\mathcal{X}_E(:, :, :, t_2, p_1)$ can be extracted by the adaptive dimensional slicing operation from the original tensor.

Using the extracted three-dimensional tensor grid structure based on spatial coordinates as the foundation for radar terrain occlusion calculations can convert irregular point data into regular grid data. This conversion turns irregularly distributed latitude and longitude coordinates into regularly distributed tensor grid indices. In subsequent calculations, tensor indices are directly used, thus avoiding complex longitude and latitude conversions and distance calculations, making spatial operations more convenient. In addition, when there are multiple radar radiation sources, the tensor addition operation can also be used to flexibly calculate the superposition effect of multiple radiation sources.

3.2. Definition of Three-Dimensional Tensor Grid Dilation Operator

Morphology is a digital image processing method based on set theory, in which a structuring element is used to perform set operations pixel by pixel in the image, ultimately obtaining the image result after morphological operations. Mathematical morphological operations commonly include erosion, dilation, opening operation, closing operation, etc. In this paper, the 3D tensor grid dilation operator is constructed from the dilation operation

in binary image morphology. The set discussed in the dilation operation in the binary image is the elements of the two-dimensional integer space Z^2 , where each element of the set is a coordinate pair corresponding to the coordinate (x, y) of the target pixel in the image [19]. Extending this notion to higher dimensions, the elements in the set are coordinate pairs that correspond to the dimensions of the tensor grid; that is, the index values of each dimension. In particular, the 3D tensor grid dilation operator is defined within the three-dimensional integer space Z^3 , and the coordinate pairs corresponding to the set are the spatial dimensional coordinates (x, y, z) .

The operands of the 3D tensor grid dilation operator include the target set and the 3D structuring element. The target set is the set to be processed, and the 3D structuring element is a predefined “template” with a certain shape used to measure and extract corresponding features. Different from the matrix form of 2D structuring elements, 3D structuring elements can be represented as a three-dimensional tensor. In general, structuring elements are usually chosen to have symmetric structures. Figure 6 shows several examples of 3D structuring elements, where the yellow grid represents the origin of the structuring element, and the blue grid represents the members of the structuring element.

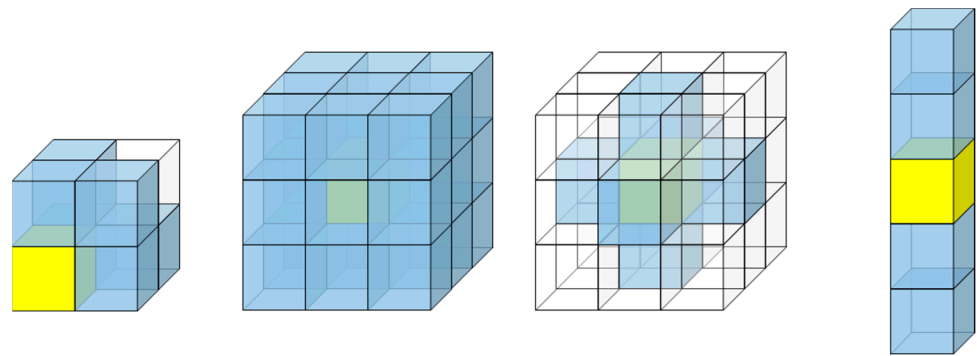


Figure 6. Several examples of 3D structuring elements.

We must define the set A and the 3D structuring element B in the three-dimensional integer space Z^3 . Before defining the 3D tensor grid dilation operator, it is necessary to define the reflection and translation of the 3D structuring element, where reflection represents the symmetric mapping of the structuring element about its origin, and translation means that the entire structuring element is shifted by a certain displacement with respect to its origin. The definitions of reflection and translation of the 3D structuring element B are as follows:

$$\hat{B} = \{w | w = -b, b \in B\}, \quad (2)$$

$$(\hat{B})_d = \{c | c = w + d, w \in \hat{B}\}, \quad (3)$$

where \hat{B} represents the reflection of B with respect to the origin, $(\hat{B})_d$ represents the translation of \hat{B} with respect to d , b represents elements in 3D structuring element B , w represents elements in \hat{B} , c represents elements in $(\hat{B})_d$, and d represents displacement vector, which can be expressed as $d = (d_x, d_y, d_z)$. After reflection, the element (x, y, z) in B becomes $(-x, -y, -z)$ in \hat{B} , and after translation, the element $(-x, -y, -z)$ in \hat{B} becomes $(d_x - x, d_y - y, d_z - z)$ in $(\hat{B})_d$.

The 3D tensor grid dilation process can be described as follows: after reflecting and translating the structuring element B by displacement d , the intersection of $(\hat{B})_d$ and set A remains a non-empty set. The mathematical expression for the 3D tensor grid dilation operator is as follows:

$$A \oplus B = \{d | [(\hat{B})_d \cap A] \neq \emptyset\}, \quad (4)$$

where \emptyset represents the empty set, $A \oplus B$ represents the dilation operation of A and B , and d represents displacement. Note that d is defined relative to the origin of \hat{B} , which is the current coordinate of the origin. In practical applications, to reduce computational

complexity, it is common to use the elements of set A as the origin positions for the 3D structuring element B , then fill the elements within it. The equation can be expressed as follows:

$$A \oplus B = \{b + a | a \in A, b \in B\}, \tag{5}$$

where a represents the elements of set A and b represents the elements of 3D structuring element B . The schematic diagram of the 3D tensor grid dilation process is shown in Figure 7, and to show it more clearly, a specific tensor slice has been chosen to demonstrate the 2D dilation process, as shown in Figure 8.

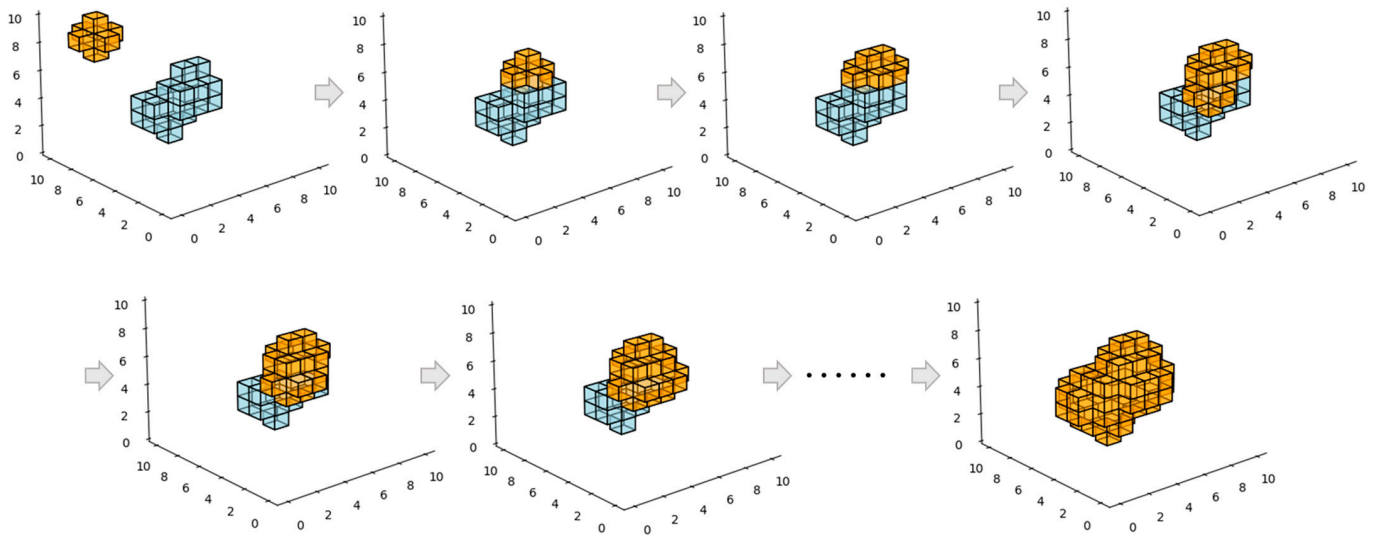


Figure 7. Schematic of 3D dilation process.

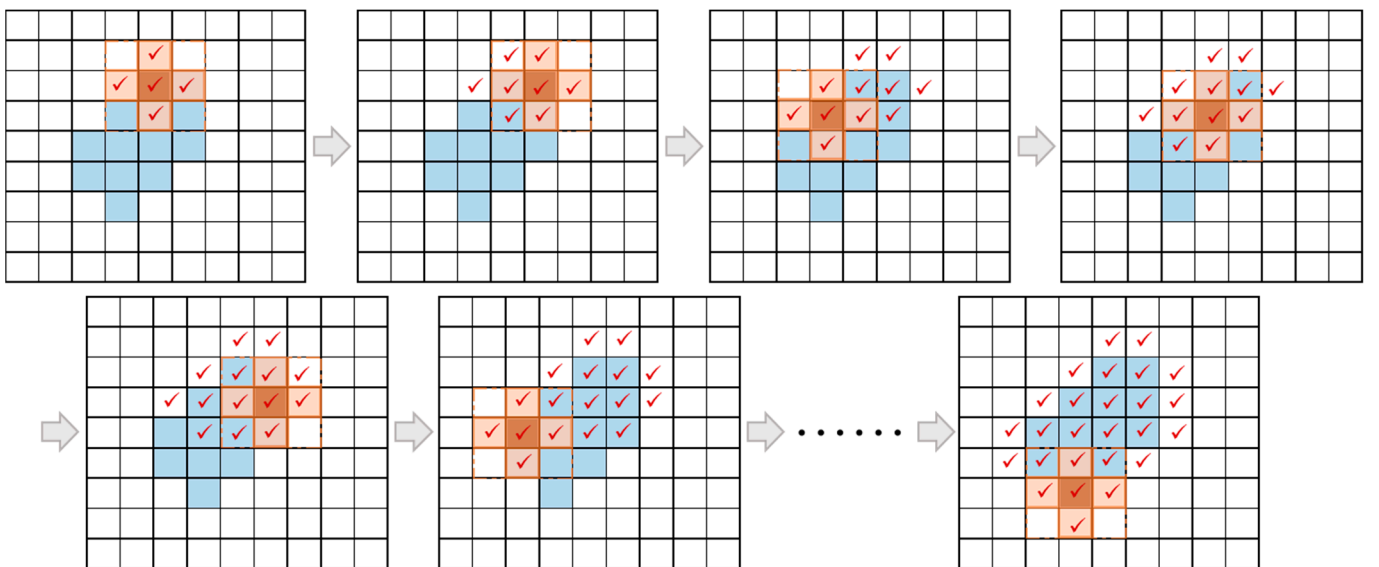


Figure 8. Schematic of 2D dilation process in a specific tensor slice.

In Figure 7, the blue grids represent the original grids set, while the orange grids represent the 3D structuring element and the results after dilation. In Figure 8, the blue grids represent the two-dimensional slice of the original grids set, the orange grids represent the two-dimensional slice of the 3D structuring element, and the red checkmarks indicate the results after dilation.

3.3. Definition of Added Points Calculation for Three-Dimensional Tensor Grid Dilation Operator

When the dilation is performed consecutively, since the result after dilation includes the set before dilation, if each dilation operation uses the result from the previous dilation operation as the target set, it will result in many repetitive calculations for the displacement d , thereby increasing the computational complexity. Therefore, in this case, we can calculate the set of added points during each dilation operation and use it as the target set for the next dilation operation.

We let the set of added points be C , then $C = A \oplus B - A$. As the dilation progresses, each dilation operation is performed based on the set of added points obtained from the previous dilation. The set of added points C_n for the n th dilation can be expressed as follows:

$$C_n = C_{n-1} \oplus B - A \cup \left(\bigcup_{i=1}^{n-1} C_i \right) = C_{n-1} \oplus B - A \cup C_1 \cup \dots \cup C_{n-1}, \quad (6)$$

In order to provide a clearer illustration of the set of added points, a two-dimensional dilation is shown as an example in Figure 9. The calculation of the set of added points for three-dimensional dilation follows a similar approach.

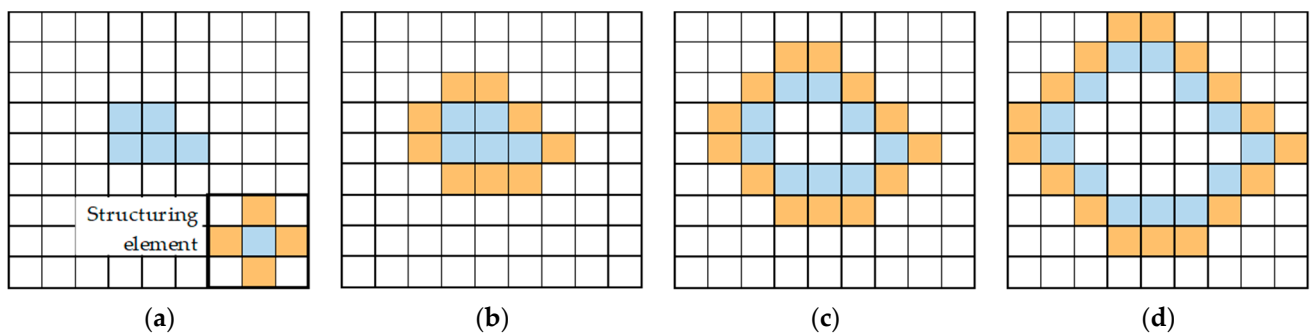


Figure 9. Schematic of the set of added points for two-dimensional successive dilation. (a) Original grid set with structuring element; (b) Result of the first dilation; (c) Result of the second dilation; (d) Result of the third dilation.

In the above diagram, the blue grids represent the target set for the current dilation operation, the orange grids represent the set of added points for the current dilation operation, and the bottom right corner in (a) shows the structuring element used for dilation. The first dilation operation is based on the original grid set. From the second dilation operation onwards, the target set for each dilation is the set of added grids obtained from the previous dilation operation, and the set of added grids for the current operation is computed according to Equation (6).

4. Radar Terrain Masking Calculation Algorithm Based on Three-Dimensional Tensor Grid Dilation Operator

To calculate the radar terrain masking, an algorithm based on the 3D tensor grid dilation operator has been developed. The algorithm dilates outward from the overlapping region between the ideal radar detection range and the terrain. It then adjusts the dilation process using the dilation judgment factor, so as to obtain the area of radar occluded by terrain as well as the actual detection range. The algorithm enables focusing on the radar's internal characteristics while considering the boundary of its detection range. The overall algorithmic flow chart is illustrated in Figure 10.

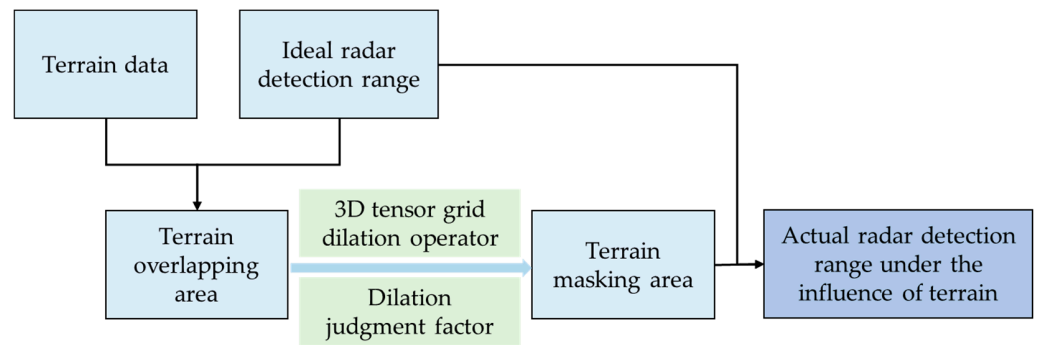


Figure 10. The overall algorithmic flow chart.

4.1. Definition of Data Structure

The electromagnetic tensor grid data model in this paper does not consider the time dimension, and the property dimension includes the power value and the type flag of the location, which is expressed as follows:

$$\mathcal{X}_E \in R^{I_1 \times I_2 \times I_3 \times I_P}, \tag{7}$$

where I_{1-3} represents the three spatial dimension sizes of longitude, latitude, and altitude, respectively, and I_P represents the property dimension size, in this case $I_P = 2$. The type flags include “0, 1, 2, 3”, where “0” indicates that the grid has not yet been calculated, “1” indicates that the grid belongs to the calculated actual radar detection range, “2” indicates that the grid is the boundary of the ideal radar detection range, and “3” indicates that the grid belongs to the terrain set. The details are shown in Table 1.

Table 1. Type flags and meanings.

Type Flag	Expressed Meaning
0	The grid has not yet been calculated
1	The grid belongs to the calculated actual radar detection range
2	The grid is the boundary of the ideal radar detection range
3	The grid belongs to the terrain set

Since the power values in the property dimension are not used in the calculation, an adaptive dimensional slicing operation is performed on the electromagnetic tensor grid data model \mathcal{X}_E , to extract the remaining dimension involved in the calculation, i.e., the type flag dimension. This process results in a new tensor, as follows:

$$\mathcal{X} \in R^{I_1 \times I_2 \times I_3}, \tag{8}$$

For subsequent calculations, the ideal radar detection range is stored in set S_{Rader} , the boundary of the ideal radar detection range is stored in set $S_{Boundary}$, and the terrain data are stored in set $S_{Terrain}$. These sets can be represented with type flags, as follows:

$$\begin{cases} S_{Boundary} = \{ (i, j, k) | \mathcal{X}_{ijk} = 2 \} \\ S_{Terrain} = \{ (i, j, k) | \mathcal{X}_{ijk} = 3 \} \end{cases}, \tag{9}$$

4.2. Dilation Judgment Factor

Before proposing the dilation judgment factor, it is necessary to assess the terrain masking situation. For this purpose, a terrain occlusion judgment method is proposed. For any spatial grid P , the first step is to construct a 3D line segment connecting the radiation source and the spatial grid P . The tensor grid indices are used as the coordinates of the points on the line segment. The Three-Dimensional Digital Differential Analyzer (3D-DDA) algorithm [20] is utilized to achieve the construction of the line segment, i.e., the passing

grids are recorded gradually from the grid where the radiation source is located along the direction of the connecting line, and the grids are then stored in the 3D line segment set S_{Line} . Whether this spatial grid is occluded or not is determined by judging whether there is an intersection between the 3D line segment and the terrain set $S_{Terrain}$. If there is an intersection between two sets, the spatial grid is considered occluded by the terrain; therefore, the occlusion factor $F_{occlusion} = 1$. If there is no intersection, the spatial grid is considered to be un-occluded, and $F_{occlusion} = 0$. For spatial grid P , the occlusion factor is calculated as follows:

$$F_{occlusion} = \begin{cases} 1, & \text{if } S_{line_P} \cap S_{Terrain} \neq \emptyset \\ 0, & \text{if } S_{line_P} \cap S_{Terrain} = \emptyset \end{cases} \quad (10)$$

where S_{line_P} represents the set of spatial grids in the 3D line segment connecting spatial grid P to the radiation source and $S_{Terrain}$ represents the set of terrain data. The schematic diagram of terrain occlusion judgment is shown in Figure 11, where the red grid represents the radiation source, the green grid represents the grid to be judged, and the blue grids represent the terrain.

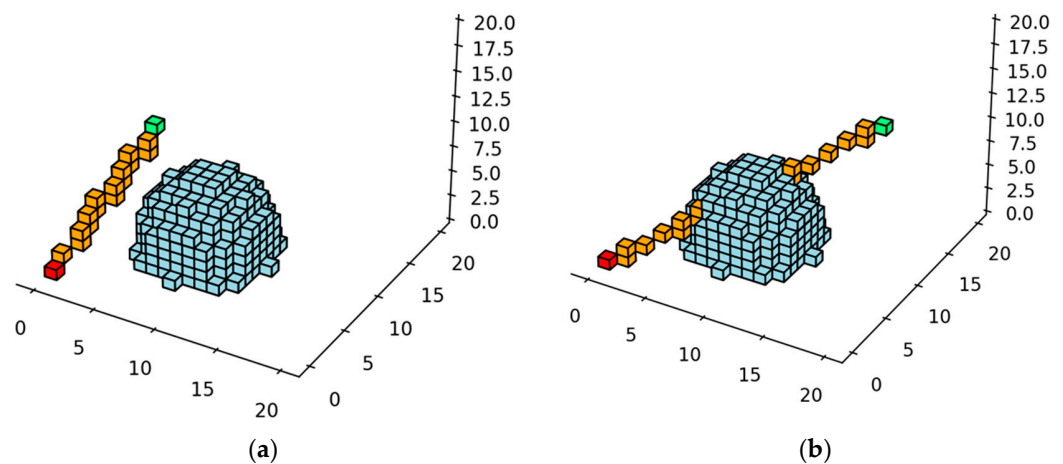


Figure 11. Schematic diagram of terrain occlusion judgment. (a) The spatial grid is not obscured; (b) The spatial grid is obscured.

On this basis, the dilation judging factor F_{Judge} is further proposed to judge whether the dilation should be performed towards a certain spatial grid $P(p_x, p_y, p_z)$. When the spatial grid P meets one of the following conditions, the dilation judging factor $F_{Judge} = 0$:

- (1) The current spatial grid P coincides with the terrain set; that is, $P \in S_{Terrain}$;
- (2) The current spatial grid P belongs to the boundary; that is, $P \in S_{Boundary}$;
- (3) The current spatial grid P is not occluded by the terrain: that is, $S_{line_P} \cap S_{Terrain} = \emptyset$,

$F_{occlusion} = 0$.

Conversely, if the spatial grid P does not coincide with the terrain, does not belong to the boundary, and is occluded by the terrain, i.e., when $P \notin S_{Terrain}$, $P \notin S_{Boundary}$, and $F_{occlusion} = 1$ are satisfied, the judgment factor $F_{Judge} = 1$.

4.3. Algorithm Flow

The radar terrain masking calculation algorithm based on 3D tensor grid dilation operator firstly represents the ideal radar detection range and terrain as a set, respectively, and then dilates outwards from the terrain overlapping area. The specific algorithm flow is as follows, and the flow chart is shown in Figure 12.

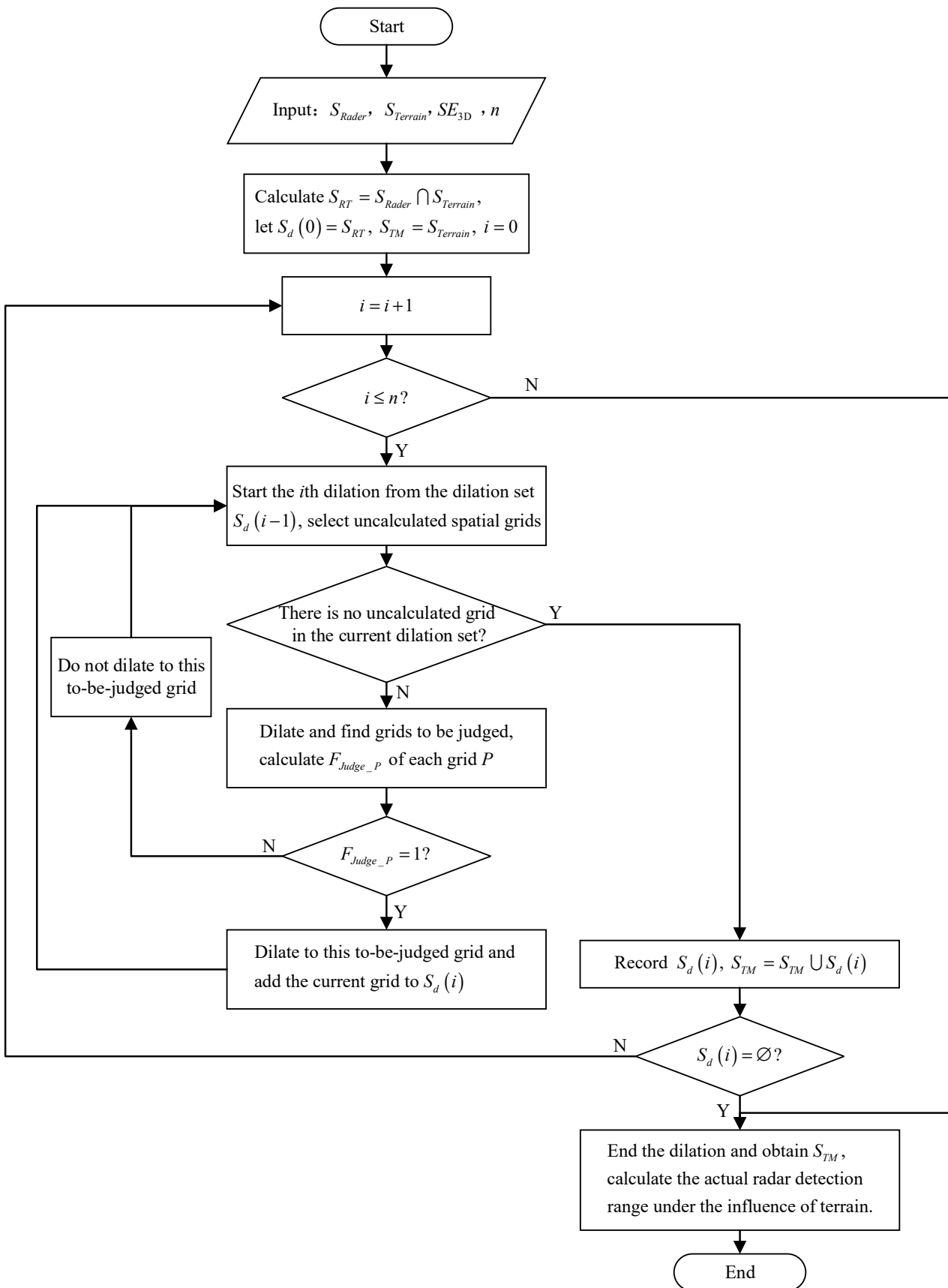


Figure 12. Algorithmic flow chart.

Step 1. Calculate the intersection S_{RT} of the ideal radar detection range set S_{Rader} and the terrain set $S_{Terrain}$, which overlap the radar detection range and terrain under ideal conditions. Let the initial set of dilation $S_d(0) = S_{RT}$, set the terrain masking set $S_{TM} = S_{Terrain}$, the 3D structuring element SE_{3D} , the maximum number of iterations n , and the number of dilation iteration count $i = 0$.

Step 2. Set the dilation iteration count $i = i + 1$. If $i \leq n$, turn to **Step 3**; if $i > n$, turn to **Step 8**.

Step 3. Start the i th dilation from the current dilation set $S_d(i - 1)$, select the uncalculated spatial grid P in the dilation set. If there is no uncalculated grid in the current dilation set, turn to **Step 7**; otherwise, turn to **Step 4**.

Step 4. Dilate based on the 3D tensor grid dilation operator with 3D structuring element $3D-SE$ and obtain the added grids, which are defined as to-be-judged grids. Calculate the dilation judging factor F_{Judge_P} of each grid P , if $F_{Judge_P} = 1$, turn to **Step 5**; if $F_{Judge_P} = 0$, then turn to **Step 6**.

Step 5. Dilate to this to-be-judged grid and add the current grid to the added dilation set $S_d(i)$ and turn to **Step 3**.

Step 6. Do not dilate to this to-be-judged grid, and the current grid is not added to the added dilation set, turn to **Step 3**.

Step 7. Record the current added dilation set $S_d(i)$, find the union set of $S_d(i)$ and the terrain masking set S_{TM} , and determine whether $S_d(i)$ is the empty set. If $S_d(i) \neq \emptyset$, turn to **Step 2**, and if $S_d(i) = \emptyset$, turn to **Step 8**;

Step 8. End the dilation to obtain the terrain masking set S_{TM} . Then, calculate the actual radar detection range under the influence of terrain, based on the ideal radar detection range.

5. Experiments and Results

In this section, the radar detection range under ideal conditions is calculated by the radar equation as initial data, and several experiments are carried out on this basis.

5.1. Experimental Data

According to the radar equation [21], the maximum detection range of the radar with a transmitter/receiver shared antenna is expressed as follows:

$$R_{\max} = \left[\frac{P_t G^2 \lambda^2 \sigma}{(4\pi)^2 S_{\min}} \right]^{1/4}, \quad (11)$$

where P_t represents the radar transmit power, G represents the radar antenna gain, λ represents the radar operating wavelength, σ represents the target radar cross-section, S_{\min} represents the minimum detectable signal power, and its expression is as follows:

$$S_{\min} = kT_0 B_n F_n (S/N)_{\min}, \quad (12)$$

where k is the Boltzmann constant, T is the standard room temperature (it generally takes 290 K), B_n represents the receiver noise bandwidth, F_n represents the noise factor, and $(S/N)_{\min}$ represents the minimum output signal-to-noise ratio required to detect the target signal, also known as the detectability factor D_o .

Under ideal conditions, the maximum detection range of radar in the determined direction of elevation θ and azimuth φ is as follows:

$$R(\theta, \varphi) = R_{\max} \times F(\theta, \varphi), \quad (13)$$

where $F(\theta, \varphi)$ is the radiation pattern of the antenna. In this paper, the Gaussian pattern is adopted in data simulation, and the bidirectional working Gaussian function is approximately expressed as follows:

$$F(\theta) \approx e^{-2.8 \frac{\theta^2}{\theta_{0.5}^2}}, \quad (14)$$

The ideal radar detection range in the experimental data of this paper is calculated from the radar equation of Equations (11)–(14). Radar parameters are shown in Table 2.

Table 2. Radar parameters.

Radar Parameter	Value
Radiation source location	(24°N, 115°E)
Radiation source altitude	400 m
Transmit power	50 kW
Antenna gain	10
Radar operating frequency	1 GHz
Radar operating wavelength	0.3 m
Half-power beamwidth	30°
Target radar cross-section	10 m ²
Minimum output Signal-to-Noise Ratio (SNR)	20 dB

This paper uses the global subdividing grid as a foundation. Currently, a representative example is the “geographical coordinates subdividing grid with one-dimension integral coding on 2ⁿ-Tree”, referred to as GeoSOT [22]. Therefore, we chose to experiment with GeoSOT-3D subdivision framework, which is the three-dimensional extension of GeoSOT. Based on the aforementioned experimental parameters, the ideal radar detection range is calculated, and the spatial subdivision is carried out according to the GeoSOT-3D subdivision framework. The radar detection range under ideal conditions and its representation with subdividing grids are shown in Figure 13.

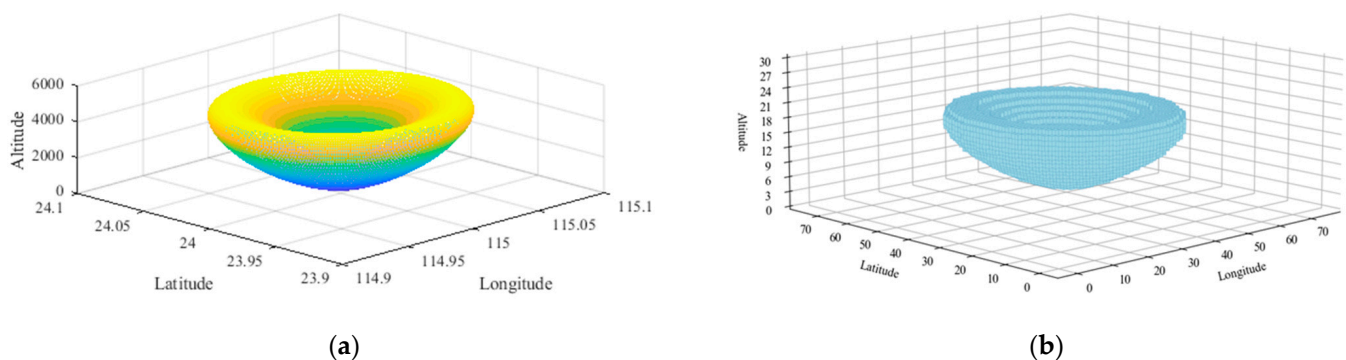


Figure 13. Radar detection range under ideal conditions. (a) Radar detection range in geographic coordinates; (b) radar detection range displayed by subdividing grids.

5.2. Experimental Results and Discussions

To verify the feasibility of the algorithm, three simulated terrain datasets with different shapes are designed, and a series of experiments are conducted. The software configuration for the experiment is Python 3.9 and Visual Studio 2019.

Firstly, experiments are conducted separately on three simulated terrain datasets for validation. Then, experiments are performed on Dataset 1 under different subdivision layers and grid sizes, with a comparison of the calculation time at each layer. Subsequently, we compare the calculation time of our algorithm with the line-of-sight visibility detection method [8]. Finally, experimental validation is performed under real terrain data.

5.2.1. Experimental Results of Two Simulated Terrain Datasets

Three shapes of simulated terrain datasets are designed. Dataset 1 has the shape of a hemisphere, located 5 km east of the radar radiation source with a radius of 2.5 km. Dataset 2 is shaped like a tetrahedron, located 4.5 km east of the radar radiation source with a height of 2.5 km and a bottom side length of 5 km. Dataset 3 is a more complex bimodal terrain located east of the radiation source. The spatial relationship between the simulated terrain

and the radar detection range, as well as the experimental results, are shown in Figure 14. In Figure 14, the green grids represent the simulated terrain and the cyan grids represent the actual radar detection range under terrain occlusion. Specific experimental results are shown in Table 3. The experiments are conducted with Layer 17, and the corresponding grid sizes are shown in Table 4.

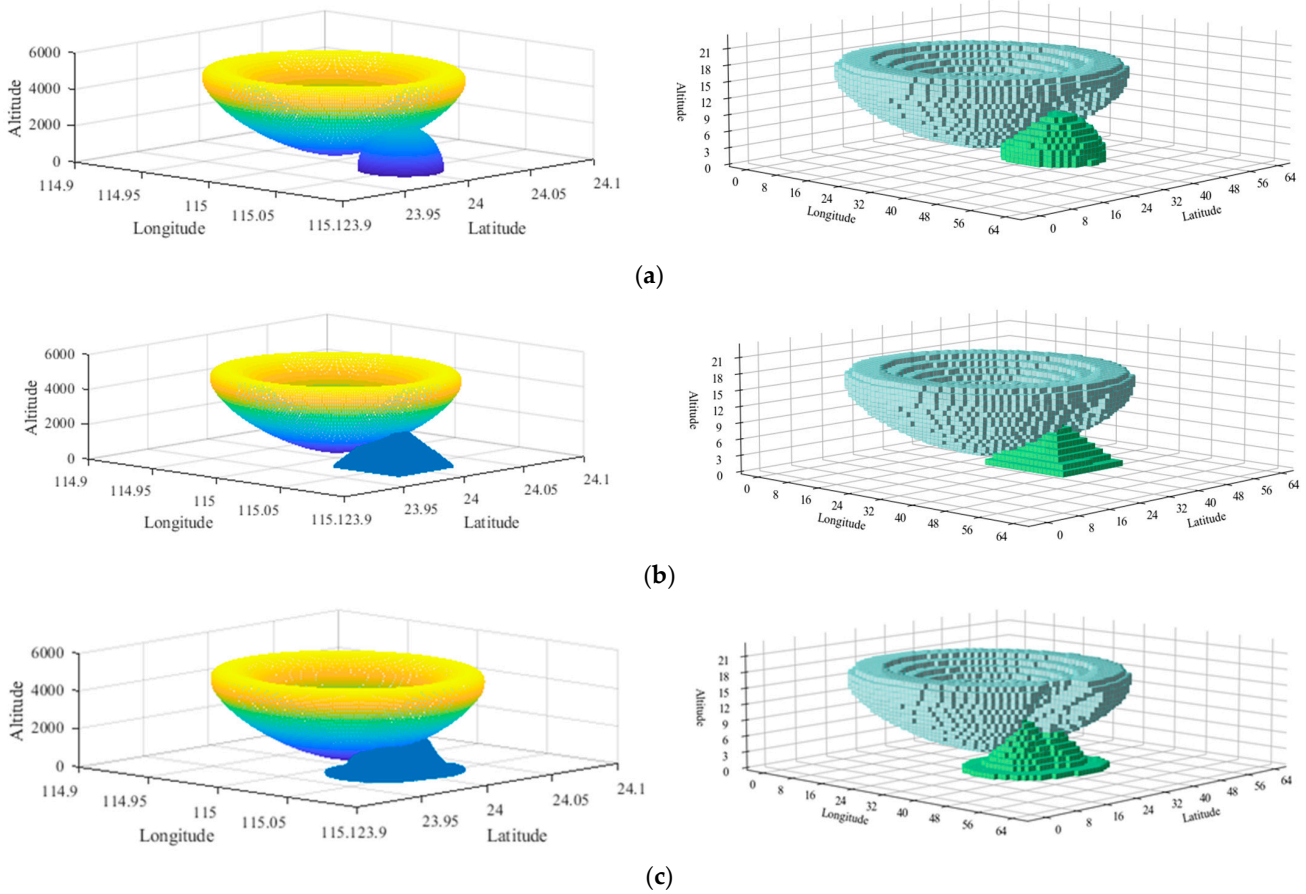


Figure 14. The spatial location relationship between the simulated terrain, radar detection range, and experimental results. (a) Simulated terrain dataset 1 and experimental results; (b) simulated terrain dataset 2 and experimental results; (c) simulated terrain dataset 3 and experimental results.

Table 3. Specific experimental results of two simulated terrain datasets.

Simulated Terrain Datasets	Number of Terrain Grids	Number of Intersecting Grids	Number of Masking Grids	Calculation Time
Dataset 1	1382	271	706	0.143 s
Dataset 2	959	127	361	0.093 s
Dataset 3	1153	151	1092	0.230 s

Table 4. Experimental results of different subdividing layers and grid sizes.

Subdivision Layer	Grid Size	Total Number of Grids	Number of Intersecting Grids	Number of Masking Grids	Calculation Time
15	1280 m	433	22	63	0.006 s
16	640 m	2558	72	300	0.034 s
17	320 m	15,987	271	706	0.143 s
18	160 m	115,223	1566	4061	1.139 s
19	80 m	873,155	10,106	20,734	9.124 s

Among them, the number of terrain grids refers to the number of grids obtained after subdividing the simulated terrain, the number of intersecting grids refers to the number of grids in the part of the simulated terrain overlapping with the radar detection range, and the number of masking grids is the number of grids in the part of the terrain affected by terrain masking. From Figure 14, it can be seen that the dilation method is capable of calculating terrain occlusion under various terrain conditions. Even for more complex terrains such as multi-peak situations, it can accurately perform calculations.

5.2.2. Experimental Results Varying Subdivision Layers and Grid Sizes

To explore the relationship between calculation time and grid size, experiments are conducted based on Dataset 1, with five consecutive layers and corresponding grid sizes. The experimental results are shown in Table 4, and Figure 15 shows the results for each layer, with cyan grids representing the actual radar detection range and green grids representing the simulated terrain.

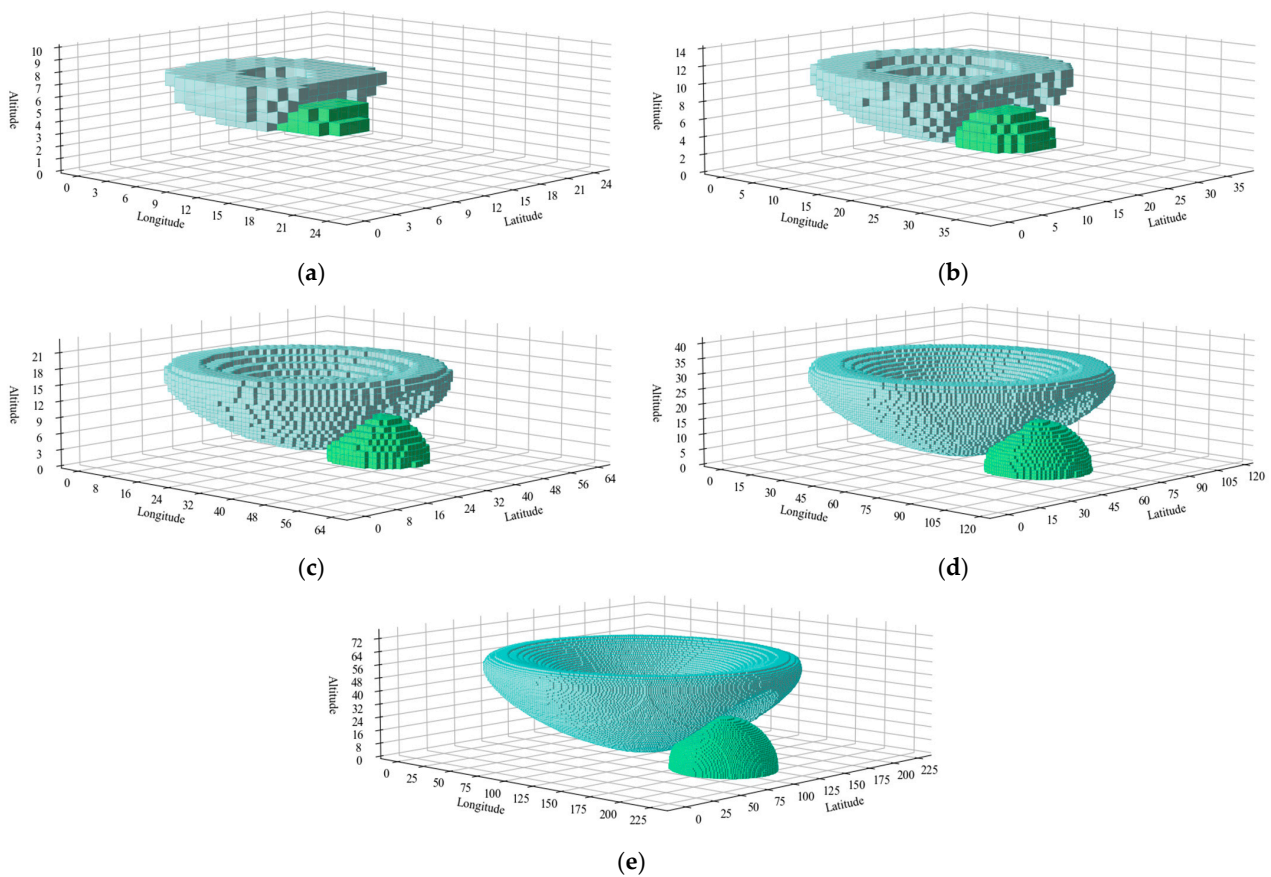


Figure 15. Experimental results of each layer. (a) Layer 15; (b) Layer 16; (c) Layer 17; (d) Layer 18; (e) Layer 19.

It can be observed that our algorithm effectively addresses terrain obstruction issues at each layer. As the layer increases, the grid size decreases gradually, leading to an exponential growth in the number of grids and, consequently, an exponential increase in calculation time. Figure 16 illustrates the trend of the logarithm base 10 of the total number of grids and the number of masking grids, as well as the calculation time as the layer increases.

It is evident that the logarithm of the number of grids increases almost linearly with the layer, i.e., the number of grids grows exponentially with the number of layers. As shown in Table 4, the number of grids increases exponentially with the increase in layers, while the calculation time exhibits a similar growth trend. When refining from Layer 18 to

Layer 19, the number of grids increases nearly sevenfold from 115,223 to 873,155, and the calculation time also increases sevenfold, resulting in a significant surge in calculation time.

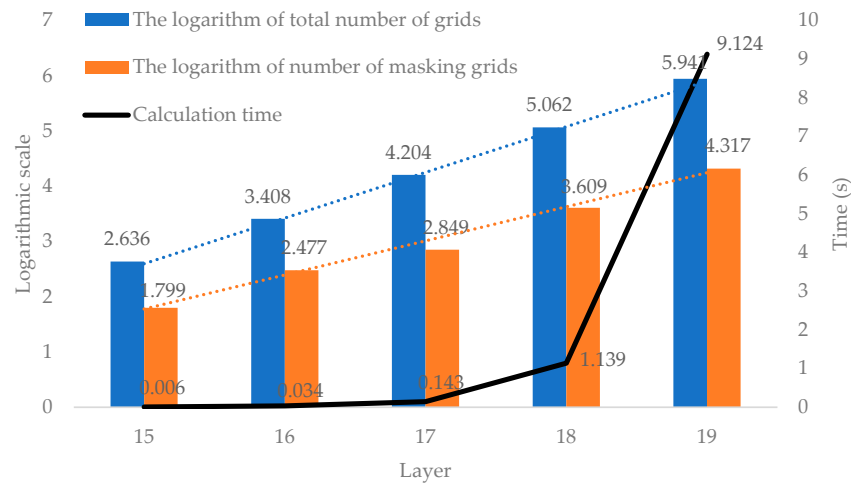


Figure 16. The trend of the logarithm base 10 of the total number of grids and number of masking grids and calculation time.

5.2.3. Comparison of Computational Efficiency and Accuracy with Existing Algorithms

Currently, two commonly used methods are the ray propagation method and the line-of-sight visibility algorithm. The ray propagation method corrects the detection range boundary by utilizing the principle of ray propagation within vertical profiles. However, this approach does not consider internal conditions, resulting in faster but less precise calculations. The line-of-sight visibility method samples at specific intervals within vertical profiles and determines whether the sampling point is occluded by comparing elevation angles with the terrain. Therefore, the calculation time of our algorithm is compared with the line-of-sight visibility algorithm at Layer 17. In the line-of-sight visibility method, the azimuth angle sampling interval is 2° , and the vertical profile sampling interval is $300\text{ m} \times 300\text{ m}$, which is similar to the grid size at Layer 17. The sampling method for the line-of-sight visibility method is illustrated in Figure 17, where * in (b) denote the sampling points.

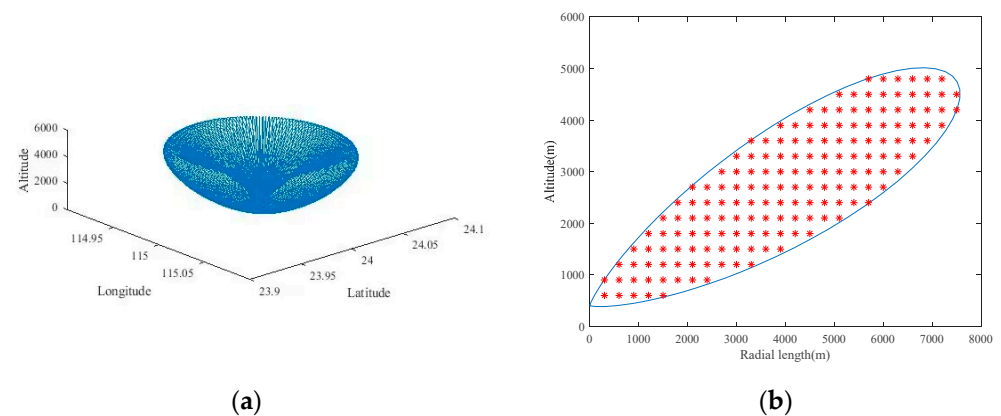


Figure 17. Sampling method for line-of-sight visibility method. (a) Sampling method in the azimuthal direction; (b) sampling method in a vertical profile.

To validate the accuracy of the dilation method, the results of the dilation method are compared with those of the line-of-sight visibility method. Since the line-of-sight visibility method evaluates each sampling point on the vertical profiles, it serves as the benchmark for comparison. The relative error is calculated as follows:

$$\varepsilon = \frac{|Num_D - Num_L|}{Num_L} \times 100\%, \quad (15)$$

where ε represents the relative error, Num_D denotes the number of grids of the actual radar detection range obtained by the dilation method, and Num_L denotes the number of grids of the actual radar detection range obtained by the line-of-sight visibility method. The comparison results are shown in Table 5.

Table 5. Comparison results of calculation time and accuracy between current algorithm and existing algorithms.

	Dilation Method Calculation Time	Line-of-Sight Visibility Method Calculation Time	Relative Error
Dataset 1	0.143 s	0.338 s	1.29%
Dataset 2	0.093 s	0.597 s	0.42%
Dataset 3	0.230 s	0.406 s	0.98%

It can be observed that the relative errors of the dilation method and the line-of-sight visibility method are all within 1.5%, which is relatively small. Moreover, the dilation method significantly reduces computation time compared to the line-of-sight visibility method, resulting in nearly a doubled increase in computational efficiency. Analysis reveals that both the dilation method and the line-of-sight visibility method consider internal points in the calculation, especially the latter method requires visibility determination for each sampling point, leading to a significant increase in calculation time. In contrast, the dilation method utilizes dilation judgment factors to skip computation for some grids when calculating the occlusion case, thereby improving computational efficiency. Additionally, the line-of-sight visibility method oversamples positions close to the radiation source due to azimuthal sampling, resulting in computational redundancy, which is not an issue with the tensor grid method.

5.2.4. Experimental Results with Actual Digital Elevation Model (DEM) Data

In order to validate the adaptability of our algorithm to real terrain, actual digital elevation model (DEM) data are imported, with the center at (24°N, 115°E) and the simulated area spanning from (23.9°N, 114.9°E) to (24.1°N, 115.1°E), as shown in Figure 18. The experiment is carried out at Layer 17, with 74 intersecting grids and 479 masking grids, and the calculation time is 0.088 s. The experimental result is illustrated in Figure 19, where the green grids indicate the terrain and the cyan grids indicate the actual radar detection range under terrain occlusion. It can be seen that the algorithm in this paper can be applied to actual terrain.

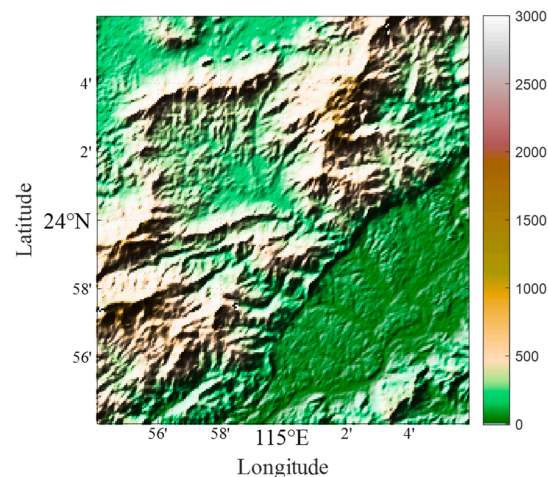


Figure 18. Elevation map of the simulation area.

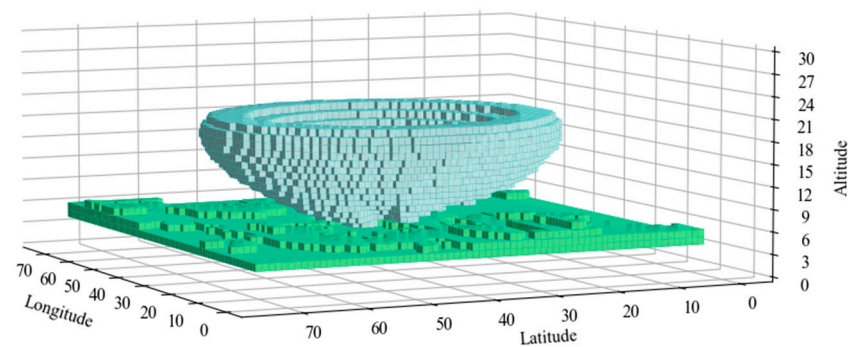


Figure 19. The experimental result under actual terrain.

6. Conclusions

To address the issue of radar detection range being affected by terrain masking, this paper proposes a radar terrain masking calculation model based on the tensor grid dilation operator. The algorithm first performs grid subdivision of the high-dimensional electromagnetic data and constructs the tensor grid model. Then, it calculates terrain masking using the idea of the dilation operation in morphology. This algorithm can calculate terrain masking with various terrain shape characteristics and at different grid sizes, significantly improving computational efficiency while focusing on internal features of the radar detection range.

The research in this paper is limited to terrain masking calculations within the horizontal plane of the Earth, ignoring the influence of the curvature of the Earth. Meanwhile, the research primarily focuses on computing the radar coverage range at a specific moment and does not consider cases where the position or parameters of the radiation source vary over time. In future research, we will consider additional factors such as the curvature of the Earth, atmospheric attenuation, and electromagnetic wave diffraction. Furthermore, leveraging the high-dimensional properties of tensors will be crucial for computing the actual radar detection range when the radiation source undergoes dynamic changes.

Besides, we will also explore the relationship between the actual requirements and the grid size, which can guide the user in choosing the best parameters for their specific applications. For example, when the radiation source is fixed, priority can be given to computation accuracy by selecting a finer grid size. However, when the radiation source varies, priority should be given to computational efficiency, even if it means sacrificing some computational accuracy.

Author Contributions: Conceptualization, B.C., X.W. and S.F.; methodology, K.N., X.W. and B.C.; software, K.N. and Y.Z.; validation, B.C. and K.N.; formal analysis, B.C. and K.N.; resources, B.C.; data curation, K.N. and J.Y.; writing—original draft preparation, K.N.; writing—review and editing, K.N., B.C., Q.K. and H.L.; visualization, K.N.; supervision, B.C.; project administration, B.C.; funding acquisition, B.C. and H.L. All authors have read and agreed to the published version of the manuscript.

Funding: This research was funded by the National Key Research and Development Program of China, grant number 2022YFD2401202; the National Key Research and Development Program of China, grant number 2022YFF0503904; the Guangdong Basic and Applied Basic Research Foundation, grant number 2022A1515010113; the Shenzhen Higher Education Institutions Stabilization Support Program Project, grant number GXWD20220811163556003; the National Defense Basic Scientific Research Funds, grant number 2022-JCJQ-JJ-0287; and the Shandong Natural Science Foundation, grant number ZR202209130044.

Data Availability Statement: Data are contained within the article.

Conflicts of Interest: Author Jianpeng Yang was employed by the company ShanDong StarSAT Technology Co., LTD. The remaining authors declare that the research was conducted in the absence of any commercial or financial relationships that could be construed as a potential conflict of interest.

References

1. Chen, P.; Wu, L. 3D representation of Radar coverage in complicated environment. *Simul. Model. Pract. Theory* **2008**, *16*, 1190–1199. [[CrossRef](#)]
2. Cheng, Z.; Yin, K.; Ye, Q.; Wang, Q. Research of Radar Actual Detection Range Based on Neural Network. *Ship Electron. Eng.* **2020**, *40*, 57–61.
3. Cheng, D.; Xiang, L.; Liu, S.; Jiang, W.; Song, R. Research on Visualization Method for Detection Power of Guidance and Warning Radar. In Proceedings of the 2023 IEEE 7th Information Technology and Mechatronics Engineering Conference (ITOEC), Chongqing, China, 15–17 September 2023; pp. 1148–1151.
4. Chen, P.; Wu, L.; Yang, C. Research on Representation of Radar Coverage in Virtual Battlefield Environment Considering Terrain Effect. *J. Syst. Simul.* **2007**, 1500–1503.
5. Qiu, H.; Chen, L. 3D visualization of radar coverage under considering terrain effect. *J. Electron. Meas. Instrum.* **2010**, *24*, 528–535. [[CrossRef](#)]
6. Qiu, H.; Chen, L.; Cai, H. 3D Visualization of Radar Detection Range in Complicated Environment. *J. Univ. Electron. Sci. Technol. China* **2010**, *39*, 731–736.
7. Zhang, Z.; Wan, G.; Li, F.; Liu, J. The impact of terrain shielding on electromagnetic wave propagation algorithm and a visualization study. *Eng. Surv. Mapp.* **2015**, *24*, 41–45. [[CrossRef](#)]
8. Liu, X.; Peng, S.; Nan, H.; Wang, X. Calculation of radar network detection power under terrain masking. *J. Air Force Early Warn. Acad.* **2017**, *31*, 248–252.
9. Dong, J.; Chen, H.; Liu, Y. Calculation of Radar Terrain Blind Space Based on Earth Curvature. *J. Caetit* **2021**, *16*, 408–413.
10. Yuan, Y.; Cheng, C.; Tong, X. Calculation Method of Radar Detection Range Based on Subdivision Expression Structure. *Geomat. World* **2017**, *24*, 29–36.
11. Bi, X.; Tang, X.; Yuan, Y.; Zhang, Y.; Qu, A. Tensors in Statistics. *Annu. Rev. Stat. Appl.* **2021**, *8*, 345–368. [[CrossRef](#)]
12. Li, D.; Teng, Y.; Zhou, X.; Zhang, J.; Luo, W.; Zhao, B.; Yu, Z.; Yuan, L. A tensor-based approach to unify organization and operation of data for irregular spatio-temporal fields. *Int. J. Geogr. Inf. Sci.* **2022**, *36*, 1885–1904. [[CrossRef](#)]
13. Zhang, P.; Zhang, L.; Wang, X.; Shen, F.; Pu, T.; Fei, C. Edge and Corner Awareness-Based Spatial–Temporal Tensor Model for Infrared Small-Target Detection. *IEEE Trans. Geosci. Remote Sens.* **2021**, *59*, 10708–10724. [[CrossRef](#)]
14. Liu, D.; Sacchi, M.D.; Chen, W. Efficient Tensor Completion Methods for 5-D Seismic Data Reconstruction: Low-Rank Tensor Train and Tensor Ring. *IEEE Trans. Geosci. Remote Sens.* **2022**, *60*, 1–17. [[CrossRef](#)]
15. Chen, H.; Ahmad, F.; Vorobyov, S.; Porikli, F. Tensor Decompositions in Wireless Communications and MIMO Radar. *IEEE J. Sel. Top. Signal Process.* **2021**, *15*, 438–453. [[CrossRef](#)]
16. Zhai, C.; Zhang, W.; Sun, J.; Zhu, W.; Ma, P.; Bai, Z.; Zhang, L. Multi-Dimensional Spectrum Data Denoising Based on Tensor Theory. In Proceedings of the 2021 IEEE 4th International Conference on Electronics and Communication Engineering (ICECE), Xi'an, China, 17–19 December 2021; pp. 296–300.
17. Cai, L. Research on Grid Map Model for Electromagnetic Space. Master's Thesis, Peking University, Beijing, China, 2021.
18. Kolda, T.G.; Bader, B.W. Tensor Decompositions and Applications. *SIAM Rev.* **2009**, *51*, 455–500. [[CrossRef](#)]
19. Vizilter, Y.V.; Pyt'ev, Y.P.; Chulichkov, A.I.; Mestetskiy, L.M. Morphological Image Analysis for Computer Vision Applications. In *Computer Vision in Control Systems-1: Mathematical Theory*; Favorskaya, M.N., Jain, L.C., Eds.; Springer International Publishing: Cham, Switzerland, 2015; pp. 9–58.
20. Xiao, K.; Chen, D.Z.; Hu, X.S.; Zhou, B. Efficient implementation of the 3D-DDA ray traversal algorithm on GPU and its application in radiation dose calculation. *Med. Phys.* **2012**, *39*, 7619–7625. [[CrossRef](#)] [[PubMed](#)]
21. Gamba, J. The Radar Equation. In *Radar Signal Processing for Autonomous Driving*; Gamba, J., Ed.; Springer: Singapore, 2020; pp. 15–21.
22. Hou, K.; Cheng, C.; Chen, B.; Zhang, C.; He, L.; Meng, L.; Li, S. A Set of Integral Grid-Coding Algebraic Operations Based on GeoSOT-3D. *ISPRS Int. J. Geo-Inf.* **2021**, *10*, 489. [[CrossRef](#)]

Disclaimer/Publisher's Note: The statements, opinions and data contained in all publications are solely those of the individual author(s) and contributor(s) and not of MDPI and/or the editor(s). MDPI and/or the editor(s) disclaim responsibility for any injury to people or property resulting from any ideas, methods, instructions or products referred to in the content.